Single-vesicle imaging reveals lipid-selective and stepwise membrane disruption by monomeric a-synuclein

Single-vesicle imaging reveals lipid-selective and stepwise membrane disruption by monomeric α-synuclein

Jonas K. Hannestad[a,1], Sandra Rocha[b,1], Björn Agnarsson[a], Vladimir P. Zhdanov[a,c], Pernilla Wittung-Stafshede[b,2], and Fredrik Höök[a,2]

[a]Division of Nano and Biological Physics, Department of Physics, Chalmers University of Technology, Gothenburg 41296, Sweden; [b]Division of Chemical Biology, Department of Biology and Biological Engineering, Chalmers University of Technology, Gothenburg 41296, Sweden; and [c]Boreskov Institute of Catalysis, Russian Academy of Sciences, Novosibirsk 630090, Russia

Edited by William F. DeGrado, University of California, San Francisco, CA, and approved May 7, 2020 (received for review August 22, 2019)

The interaction of the neuronal protein α-synuclein with lipid membranes appears crucial in the context of Parkinson's disease, but the underlying mechanistic details, including the roles of different lipids in pathogenic protein aggregation and membrane disruption, remain elusive. Here, we used single-vesicle resolution fluorescence and label-free scattering microscopy to investigate the interaction kinetics of monomeric α-synuclein with surface-tethered vesicles composed of different negatively charged lipids. Supported by a theoretical model to account for structural changes in scattering properties of surface-tethered lipid vesicles, the data demonstrate stepwise vesicle disruption and asymmetric membrane deformation upon α-synuclein binding to phosphatidylglycerol vesicles at protein concentrations down to 10 nM (~100 proteins per vesicle). In contrast, phosphatidylserine vesicles were only marginally affected. These insights into structural consequences of α-synuclein interaction with lipid vesicles highlight the contrasting roles of different anionic lipids, which may be of mechanistic relevance for both normal protein function (e.g., synaptic vesicle binding) and dysfunction (e.g., mitochondrial membrane interaction).

α-synuclein | single-vesicle scattering | lipid vesicle | membrane interaction

Parkinson's disease (PD) is the second most common neurodegenerative disorder and the most frequent movement disorder today for which there is only symptomatic treatment (1, 2). Assembly of α-synuclein protein into oligomers and amyloid fibrils has been linked to the molecular basis of PD, with α-synuclein amyloids being the major content of pathological neuronal inclusions, the Lewy bodies, found in PD patient brain cells (3–5). Duplications, triplications and point mutations in the α-synuclein gene are linked to familial PD cases (6). Despite the key role of α-synuclein in emergence and progression of PD, the details of its function remain unknown, but it appears related to synaptic vesicle release and trafficking, regulation of enzymes and transporters, and control of the neuronal apoptotic response (7–9). In accord, α-synuclein, comprising 140 amino acid residues and with a molecular weight of about 14 kDa, is localized at presynaptic nerve terminals associated with synaptic vesicles (10–12). The protein has also been shown to associate with membranes of mitochondria and endoplasmic reticulum and occurs under physiological conditions in both an intrinsically unstructured form in the cytosol and a helical state on lipid membranes (13, 14). The intracellular concentration of α-synuclein is likely in the low nanomolar range, but may vary between brain cell types and between intracellular regions. Extracellularly, higher (micromolar range) concentrations of the protein have been estimated, for example, in presynaptic terminals (15).

Recent advancements in bioanalytical techniques have brought the understanding of molecular mechanisms of α-synuclein membrane toxicity forward. Fluorescence resonance energy transfer combined with total internal fluorescence imaging on planar supported lipid bilayers (SLBs) revealed the extraction of lipids from the bilayer during α-synuclein aggregation (16). A similar membrane damage induced by the protein was observed by the combined use of atomic force microscopy and dual polarization interferometry (17) as well as quartz crystal microbalance with dissipation (QCM-D) monitoring combined with neutron reflectometry (18). Studies using a combination of low-angle X-ray scattering, fluorescence correlation spectroscopy, and coarse-grained molecular dynamics revealed membrane curvature-dependent binding and remodeling by α-synuclein (19). Confocal microscopy imaging of giant lipid vesicles with encapsulated truncated α-synuclein (residues 1 to 100) showed concomitant protein aggregation and membrane permeabilization (20). Stimulated emission depletion imaging and cryoelectron microscopy were combined to demonstrate a possible role of α-synuclein as a molecular bridge between adjacent membranes (7), and, presumably, the protein also promotes dilation of exocytotic fusion pores in adrenal chromaffin cells and neurons (21). These and numerous related studies have revealed that α-synuclein binds to biological membranes with different affinity depending on their

Significance

Neurodegenerative diseases are increasing among the world's population, but there are no cures. These disorders all involve proteins that assemble into amyloid fibers which results in brain cell death. Evidence suggests that association of these proteins with lipid membranes is crucial for both functional and pathological roles. In Parkinson's disease, the involved protein, α-synuclein, is thought to function in trafficking of lipid vesicles in the brain. In search of mechanistic origins, increasing focus is put on identifying neurotoxic reactions induced by membrane interactions. To contribute new clues to this question, we here employed a new surface-sensitive scattering microscopy technique. With this approach, we discovered that α-synuclein perturbs vesicles in a stepwise and lipid-dependent fashion already at very low protein coverage.

Author contributions: J.K.H., S.R., B.A., P.W.-S., and F.H. designed research; J.K.H., S.R., B.A., V.P.Z., and F.H. performed research; B.A., V.P.Z., and F.H. contributed new reagents/analytic tools; J.K.H., S.R., B.A., V.P.Z., P.W.-S., and F.H. analyzed data; and J.K.H., S.R., B.A., V.P.Z., P.W.-S., and F.H. wrote the paper.

The authors declare no competing interest.

This article is a PNAS Direct Submission.

[1]J.H. and S.R. contributed equally to this work.

[2]To whom correspondence may be addressed. Email: pernilla.wittung@chalmers.se or fredrik.hook@chalmers.se.

This article contains supporting information online at https://www.pnas.org/lookup/suppl/doi:10.1073/pnas.1914670117/-/DCSupplemental.

lipid composition and physical properties, and has the ability to sense and change the bilayer curvature (14, 22–24) leading to drastic membrane deformation (22, 25).

Further, the protein binding affinity, either in a monomeric or aggregated state, is strongly dependent on the presence of anionic phospholipids (14, 22, 26–28). The interaction of α-synuclein with membranes is most likely relevant for both function and cellular toxicity, but, despite fairly clear indications that toxic species of α-synuclein affect cellular membranes, the molecular mechanisms underlying the membrane−protein interaction are not well understood. Besides the complex nature of the related processes, reasons for the lack of understanding include the fact that most experiments are performed either by ensemble-averaging methods or at conditions that do not enable measurements of rapid dynamics. It is, in this context, relevant to note that recent studies, based on biophysical investigations using simplified model membrane systems, suggest that membrane permeabilization observed for amyloid-forming proteins, including α-synuclein, shares key features with the significantly simpler and therefore often more well-understood process associated with pore-forming antimicrobial peptides (29). Indeed, the tremendous attention put on antibacterial peptides has offered a general understanding of the corresponding mechanistic details of the pore formation at the conceptual level and at the levels of statistical models and molecular dynamics simulations (30).

Inspired by these insights and fluorescence microscopy studies indicating that antimicrobial peptide-induced pore formation can be followed by gradual remodeling of both giant (31–34) and smaller vesicles (35), we used, in this work, a similar approach, but instead focused on the interaction of α-synuclein with surface-tethered ∼100-nm vesicles made of anionic lipids. While previous single-vesicle studies (focused on antimicrobial peptides) utilized fluorescence imaging alone (35, 36), we here employed a variant of surface-sensitive light microscopy that is capable of resolving, in both fluorescence and label-free scattering mode, individual vesicles with subsecond temporal resolution (37). This method was previously used to investigate phospholipase-induced disintegration of tethered vesicles, revealing a kinetically synchronized reduction in fluorescence and scattering intensity upon the structural changes caused by lipid digestion (37). In contrast, when lipid vesicles collapse into planar SLB patches on silica, the reduction in scattering intensity was, with this (38) and related light scattering microscopy methods (39), observed to be more dramatic than the corresponding changes in fluorescence intensity, suggesting that scattering microscopy might reveal structural alterations not easily detected by other means.

Using this combined fluorescence and scattering microscopy approach, we here investigated how α-synuclein affects the integrity of DOPS (1,2-dioleoyl-sn-glycero-3-phospho-L-serine) and DOPG (1,2-dioleoyl-sn-glycero-3-phospho-(1′-rac-glycerol)) vesicles. The aim was to explore whether protein-induced structural alterations could be detected and thereby provide molecular mechanistic insights into the kinetics of α-synuclein interaction with different lipid bilayers and resulting bilayer structural consequences. The microscopy analysis was complemented with conventional ensemble-averaging measurements using multiparametric surface plasmon resonance (MP-SPR) and QCM-D, which, combined, are particularly well suited for quantitative analysis of interfacial biomolecular interactions and investigations of structural changes of surface-bound lipid vesicles (40–42). To aid data analysis, a theoretical model representing the label-free light-scattering data was developed to account for the protein-induced stepwise (sometimes multiple steps) deformation uniquely observed for DOPG vesicles. Our discovery of strikingly different consequences of α-synuclein interactions with DOPG versus DOPS vesicles may have biological relevance given the fact that phosphatidylglycerol (PG) plays an important role in mitochondrial membranes (43, 44) whereas phosphatidylserine (PS) is found in synaptic vesicle membranes (45).

Results

α-Synuclein Changes the Viscoelastic Properties of Surface-Tethered Negatively Charged Lipid Vesicles. Before turning to single-vesicle measurements, MP-SPR and QCM-D were used to inspect time-resolved changes in mass and structural properties induced by α-synuclein binding to surface-tethered DOPG and DOPS vesicles. The vesicles were modified with a small fraction (0.25 mol %) of biotin lipids for using NeutrAvidin as a tethering linker to a poly(l-lysine)-graft-poly(ethylene glycol) (PLL-g-PEG) modified sensor surface containing 0.25% PLL-g-PEG-biotin. Upon addition of 200 nM α-synuclein to either DOPG or DOPS vesicles, there was a significant decrease in the resonance frequency shift (Δf) measured by QCM-D, which was accompanied by an increase in energy dissipation (ΔD) (Fig. 1*A*). Controls using either 1,2-dioleoyl-sn-glycero-3-phosphocholine vesicles or bare PLL-g-PEG-biotin:PLL-g-PEG surface showed no signs of α-synuclein interaction (*SI Appendix*, Fig. S1), verifying that the responses shown in Fig. 1*A* are specific.

It is, at first sight, tempting to attribute the decrease in Δf upon α-synuclein injection ($t \approx 20$ min) to an increase in coupled mass caused by protein binding to the vesicles, whereas the accompanying increase in ΔD could be associated with alterations in the structure and viscoelastic properties of the vesicles. Following this line of reasoning, the subsequent increase in Δf ($t \approx 27$ min for DOPG and $t \approx 32$ min for DOPS) could be interpreted as desorption of lipid and/or α-synuclein from the sensor surface. However, from previous studies, it is known that Δf can also be influenced by structural changes of adsorbed vesicles, which, in situations where the molecular mass remains essentially constant, are dominated by variation in the amount of coupled solvent (40).

To deconvolute changes in the bound molecular mass from coupled solvent, we used MP-SPR operated at two wavelengths. Through this technique, the interface region is probed with evanescent fields of two different decay lengths, allowing the film thickness (or the size of adsorbed particles) to be directly determined from the ratio between the corresponding responses, R_1/R_2. This, in turn, makes it possible both to identify structural changes of adsorbed vesicles and to improve the accuracy of mass quantifications (42), which were here done (see *SI Appendix*, section 3 for details) by taking into account the film thickness (*SI Appendix*, Eqs. **S1** and **S4** and Fig. S2), the difference in molecular weight between α-synuclein (∼14 kDa) and lipids (∼0.8 kDa), and the fact that proteins have a slightly higher refractive index than lipids (34, 46).

Upon addition of 200 nM α-synuclein, there was, for both DOPG and DOPS, a monotonic increase in the SPR response by around 5% (Fig. 1*B*; $t \approx 21$ min for DOPG and $t \approx 33$ min for DOPS), which corresponds to binding of ∼150 and 300 α-synuclein molecules per vesicle (assuming a nominal vesicle diameter of ∼120 nm) in the case of DOPG and DOPS, respectively (*SI Appendix*, section 3). The lower α-synuclein coverage on DOPG vesicles, despite a similar SPR response to that observed for DOPS vesicles, is explained by α-synuclein–induced vesicle contraction of the DOPG vesicles (Fig. 1*C*). Binding of α-synuclein to both types of vesicles confirms that the positive changes in Δf are indeed not due to a loss of bound lipid and/or α-synuclein, but must instead be attributed to an effect dominated by structural changes influencing the amount of water coupled to the immobilized vesicles, which are not expected to yield significant changes in the SPR response when measured at a single wavelength. It is worth noting, though, that the temporal evolution of the R_1/R_2 ratio actually differs for DOPG and DOPS vesicles upon addition of α-synuclein. For DOPG, the ratio first decreased and then increased (Fig. 1*C*, blue curve), which is indicative of an overall decrease in vesicle size (42), whereas, for

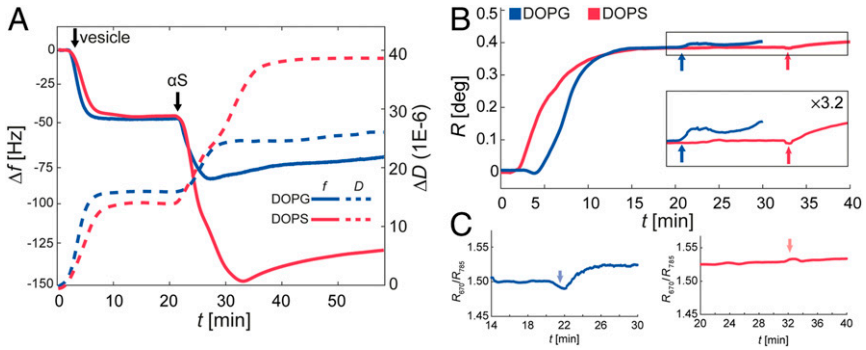

Fig. 1. QCM-D and SPR measurements of α-synuclein bound to surface-tethered lipid vesicles. (*A*) Time evolution of Δf and ΔD upon subsequent addition of lipid vesicles and α-synuclein to a PLL-g-PEG-biotin:PLL-g-PEG and NeutrAvidin-modified sensor surfaces at a PLL-g-PEG-biotin:PLL-g-PEG ratio of 0.25%. Addition of α-synuclein started after saturated binding of DOPG or DOPS vesicles and rinsing with pure buffer. (*B*) Dual wavelength SPR sensorgrams of changes in the resonance angle shift, *R*, versus time at $\lambda = 670$ nm for the same process as in *A*, for DOPG (blue) and DOPS (red) vesicles. (*C*) Time evolution of changes in the R_{670}/R_{785} ratio of the SPR response for DOPG (blue) and DOPS (red). In *B* and *C*, arrows indicate addition of α-synuclein.

DOPS, there was essentially no change in the response ratio (Fig. 1*C*, red curve), indicating that there is no measurable effect on the film thickness upon α-synuclein binding. This further supports that the measured QCM-D response is due to a combination of protein binding and protein-induced structural changes, especially for DOPG vesicles. In addition, the different features in the Δf and ΔD responses for DOPS and DOPG were even more pronounced at increasing vesicle surface coverages (*SI Appendix*, Fig. S3), suggesting that α-synuclein interaction leads to structural changes sufficiently dramatic to cause lateral interactions between adjacent vesicles.

α-Synuclein Induces Structural Remodeling of Surface-Tethered DOPG Vesicles. To gain further information on the structural changes induced upon α-synuclein binding to lipid vesicles, we performed experiments at the single-vesicle level by using a custom-built optical waveguide device that allows simultaneous surface-sensitive microscopy in fluorescence and (label-free) scattering mode (37). In this way, both the fluorescence and light-scattering emission of surface-tethered fluorescently labeled (0.25 mol % Lissamine rhodamine B 1,2-dihexadecanoyl-sn-glycero-3-phosphoethanolamine, triethylammonium salt [rhodamine DHPE]) DOPG and DOPS vesicles were monitored upon addition of α-synuclein (200 nM) under similar conditions as described above. For DOPG, the changes in the fluorescence before and after addition of α-synuclein were only minor, whereas, in label-free scattering mode, the intensity for the major fraction of the vesicles (~99%) was drastically diminished (Fig. 2 *A*–*C* and Movie S1). Although the onset of changes in scattering followed an exponential decay behavior with a time constant of ~5 s when averaged over many vesicles (Fig. 2*C*), the actual scattering intensity drop on the level of individual vesicles was essentially instantaneous in time (Fig. 2*B*, blue curves). This stepwise reduction in scattering intensity cannot be attributed to complete or partial vesicle detachment, because the corresponding fluorescence intensity remained and even increased slightly (Fig. 2*B*, red curves). Instead, this feature indicates dramatic single-step structural changes of the individual vesicles, without removal of lipid material. Notably, this result is opposed to previous observations with single-vesicle fluorescence microscopy for antimicrobial AH peptides (35) and phospholipid vesicle digestion (37). In strong contrast to the DOPG vesicles, only ~5% of the DOPS vesicles showed this type of behavior in the corresponding fluorescence and scattering emissions upon addition of α-synuclein, with the majority of the vesicles remaining essentially unaffected (Fig. 2 *C*–*E*, *SI Appendix*, Fig. S4, and Movie S2).

The extent of the reduction in the scattering intensity was rather different for distinct DOPG vesicles, and, in rare cases, the intensity even increased (Fig. 2 *B*, third panel from the *Top* and *SI Appendix*, Fig. S5). A reproducible feature that deserves further attention is that, upon exposure to α-synuclein, the scattering emission of DOPG vesicles was frequently (~60%) observed to first slightly increase before suddenly decreasing (Fig. 2 *B*, *Top* panel and *SI Appendix*, Figs. S4 and S5), with the average relative increase in scattering intensity being 0.25 (±0.18). In stark contrast, a negligible fraction of the DOPS vesicles showed a similar increase in response upon α-synuclein interaction, although the variation in the scattering signal between individual vesicles was, in that case, fairly large (0.062 ± 0.15) (*SI Appendix*, Fig. S4). In a previous study, we showed that protein binding to immobilized lipid vesicles leads to an increase in scattering intensity, ΔI_s, which, to a first approximation, scales as $r^4(d + \Delta d)^2$, where r is the vesicle radius, d ($d \ll r$) is the membrane thickness, and Δd is its increment (37). Using this relation, the analysis of the initial intensity increase upon α-synuclein addition yields, on average, only minor changes in the lipid membrane thickness ($\Delta d < 1$ nm). Judging from the scattering profile alone and this rough estimation, it might seem reasonable to attribute the increase in intensity to an increase in membrane thickness due to binding of α-synuclein to the DOPG vesicles. However, since there was almost no observable change in the scattering intensity upon binding of α-synuclein to the DOPS vesicles, and, as α-synuclein binds to both DOPG and DOPS vesicles according to MP-SPR and QCM-D, the increase in scattering observed for DOPG is more likely associated with membrane structural changes upon protein interaction. This interpretation is further supported by the fact that this feature was, for a significant fraction of the vesicles, followed by an abrupt decrease in scattering signal (Fig. 2*B* and *SI Appendix*, Fig. S5). These data also show that, for DOPG, there was no correlation in scattering intensity recorded before, t_1, and after, t_2, α-synuclein addition (Fig. 2*D*). Instead, almost all vesicles were observed to transit to a state where they scattered at a level just above the background intensity (Fig. 2*E* and *SI Appendix*, Fig. S5), with an average decrease of 90%. For DOPS, however, the scattering intensity was largely unaffected, with an average intensity decrease of only 8% (Fig. 2*E*).

In contrast to the results obtained upon addition of 200 nM α-synuclein, more diverse types of kinetics were observed in experiments with 20 times lower concentration (10 nM) of α-synuclein added (Fig. 3 and *SI Appendix*, Figs. S6–S8). Although the kinetic traces were still dominated (~95%) by a single step, abrupt decrease in scattering signal occurring ~20 to 30 s

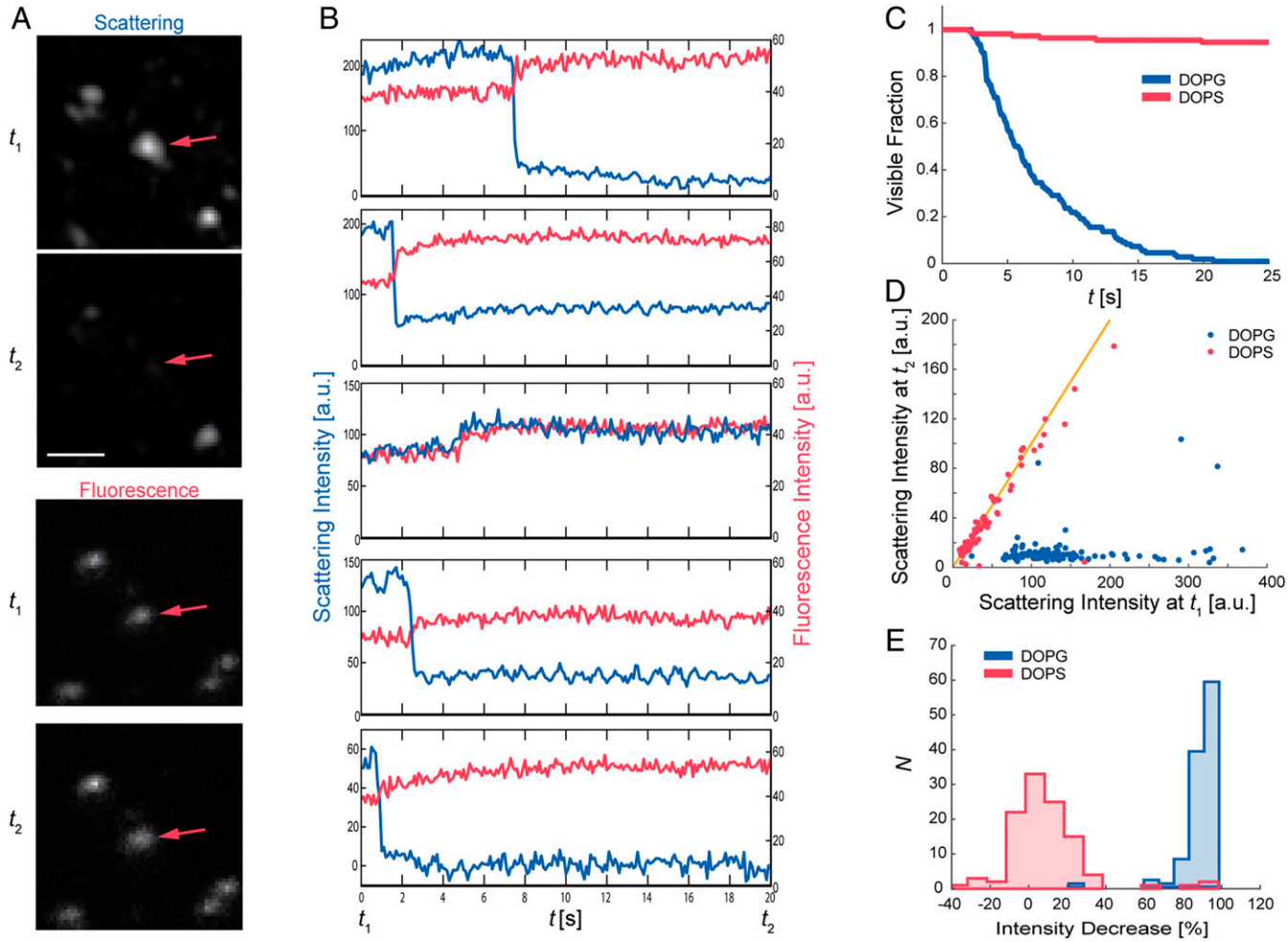

Fig. 2. Scattering and fluorescence emission from individual DOPG and DOPS vesicles. (*A*) Scattering and fluorescence images of DOPG vesicles upon (t_1) and ~20 s after (t_2) addition of α-synuclein to a final concentration of 200 nM. The red arrow indicates the same vesicle in both scattering and fluorescence micrographs. (Scale bar: 2 μm.) (*B*) Representative scattering and fluorescence intensity profiles of individual DOPG vesicles (after subtraction of dark noise). (*C*) Temporal evolution of the fraction of DOPG and DOPS vesicles that remains visible in scattering mode upon α-synuclein addition. The presented data are assembled from >100 vesicles of each type. (*D*) Scattering intensity for DOPG and DOPS vesicles at t_1 and t_2. The yellow line indicates no change in intensity between t_1 and t_2. (*E*) Integrated and normalized scattering intensity of individual DOPG and DOPS vesicles just after addition of α-synuclein (t_1) and at the end of the recording (t_2, ~20 s). The scattering background, determined at three separate spots in an area of the chip surface that did not contain any vesicles, was subtracted from the vesicle scattering profile before summation of the scattering signal associated with individual vesicles, and the area used to estimate the scattering intensity of the individual vesicles was obtained from the corresponding fluorescence images determined at the appropriate time points (see Fig. 4 and main text for elaboration on the temporal evolution of the single-vesicle fluorescence spot size).

after α-synuclein injection (Fig. 3 and *SI Appendix*, Fig. S6), and gradual and multistep decreases in scattering profiles from individual vesicles were also observed (top and middle *Right* in Fig. 3 and *SI Appendix*, Fig. S7), and, in very few cases, even a small increase or no change in scattering signals were detected (*SI Appendix*, Fig. S8). SPR could not resolve the small mass uptake at 10 nM, but the low uptake already at 200 nM (~150 α-synuclein per vesicle at saturated binding) suggests that each stepwise change is induced by significantly less than 150 α-synuclein per vesicle. In many traces, it is noteworthy that fluctuations in the scattering signal usually decrease or diminish after the α-synuclein–induced drop. Physically, the fluctuations of the scattering signal prior to α-synuclein binding are attributed to a combination of vesicle wobbling in the z direction (which, due to the evanescent illumination, results in either increase of decrease of scattering signal) and minor vesicle shape changes. It is clear from these data that α-synuclein binding also influences the dynamic of the vesicle attachment to the surface.

Fluorescence Imaging Indicates Surface Confinement of Lipids after α-Synuclein–Induced Vesicle Remodeling. While DOPG vesicles displayed drastic changes in their scattering properties, the corresponding changes in fluorescence emission were only modest. However, as already noted, the fluorescence was not entirely unaffected (Fig. 2 *A* and *B*). Fig. 4*A* shows an example of the fluorescence from individual DOPG lipid vesicles prior to ($t_1 \cong$ 0 s) and after ($t_2 \cong$ 20 s) α-synuclein addition and binding (see also Movie S1). There is a clearly discernible difference between the two micrographs, with the vesicles appearing both larger and brighter at t_2. As noted above, this is better reflected in the fluorescence intensity profiles of the vesicles, which also show how the transition between low and high intensity coincides with the reduction in scattering intensity (Fig. 2*B* and *SI Appendix*, Fig. S5). Thus, the interaction between α-synuclein and DOPG membranes leads to a change in vesicle properties that decreases the scattering signal but increases fluorescence of individual vesicles. Notably, there was no visible increase in fluorescence from DOPS vesicles upon α-synuclein addition (Movie S2). Data

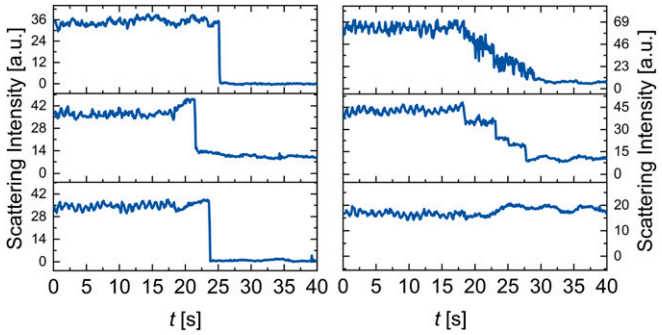

Fig. 3. Scattering emission of individual DOPG vesicles. Six representative scattering intensity profiles (after subtraction of background) of single DOPG vesicles upon exposure to 10 nM α-synuclein at $t = 0$. Difference in absolute scattering intensities between these data and Fig. 2*B* and *SI Appendix*, Figs. S4–S8 is due to differences in light intensity, chip variations, and image acquisition time. Intensity profiles were obtained using unlabeled vesicles.

for over a hundred DOPG and DOPS vesicles showed a linear relationship between fluorescence intensity before and after the transition between the states (Fig. 4*B*), but with a slope being larger than unity for DOPG. This difference is summarized in Fig. 4*C*, showing that the fluorescence change follows a normal distribution with a mean of ∼+35% and ∼−5% for DOPG and DOPS, respectively. While the minor decrease for DOPS is attributed to fluorophore bleaching, the surface-confined evanescent wave illumination of the waveguide-based microscopy used here relates the fluorescence emission primarily to the distance between lipids and surface. Hence, the experimentally observed increase in fluorescence intensity by about 30% for the DOPG vesicles (Fig. 4*C*) can be explained by assuming that the lipids become located closer to the surface after rupture. In fact, the increase observed for DOPG is in agreement with what is expected for vesicles with a nominal diameter of ∼120 nm collapsing from a spherical to a planar configuration within an evanescent field with an extension similar to the diameter of the vesicles (*SI Appendix*, section 4.2). An apparent increase in size of DOPG vesicles was also reflected in the intensity profile cross-section of the individual vesicles (Fig. 4*D*), revealing an average increase in full width at half maximum (FWHM) of 0.18 μm (Fig. 4*E*). This corresponds to an average increase in footprint diameter of ∼70%, an estimate that is certainly an underestimation, as the nominal vesicle size (prior to α-synuclein binding) is on the order of 120 nm and thus below the diffraction-limited resolution. In contrast, DOPS vesicles showed only minor changes in FWHM, with a narrow distribution centered around zero (Fig. 4*E*).

Although the changes in fluorescence intensity are moderate for DOPG and completely absent for DOPS, this analysis suggests fairly significant α-synuclein–induced structural changes of DOPG vesicles. This is interesting from the perspective of the more dramatic changes observed in the scattering than the fluorescence amplitudes. In principle, upon structural remodeling of a vesicle, the lipids can form various types of structures ranging in shape from close-packed circular patches to dispersed and anisotropic conformations. A theoretical analysis of different shapes and symmetries of patches (*SI Appendix*, section 4) demonstrates that, if a patch is compact and symmetric (e.g., circular or quadratic), the scattering intensity is predicted to either remain the same or modestly increase (*SI Appendix*, Fig. S9), which is not what we observe experimentally for most of the collapsing vesicles (Figs. 2 and 3 and *SI Appendix*, Figs. S6 and S7). In contrast, the appreciable reductions in scattering intensity frequently observed in the experiments can be explained theoretically only if the lipid patch formed after vesicle remodeling is anisotropic (e.g., rectangular or ellipsoidal) and/or adopts a dispersed shape after vesicle collapse. This interpretation of the scattering data is further supported by nanoparticle tracking analysis of suspended vesicles, which, for a significant fraction of DOPG vesicles, revealed an increase in vesicles size (reduction in diffusivity) accompanied by a dramatic decrease of their scattering intensity (*SI Appendix*, Fig. S10) ∼60 min after

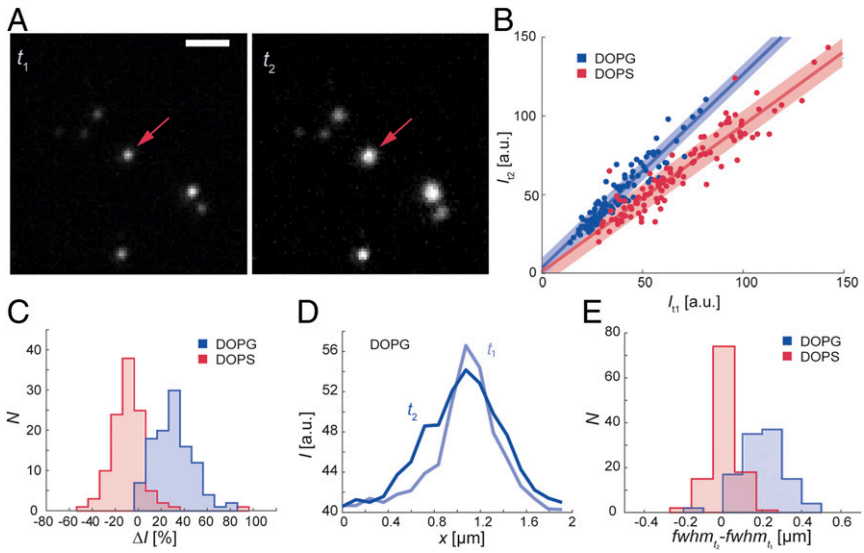

Fig. 4. Changes in single-vesicle fluorescence intensity upon addition of α-synuclein. (*A*) Fluorescence micrograph showing the same DOPG vesicles containing 1% rhodamine before ($t_1 \approx 0$ s) and after ($t_2 \approx 20$ s) addition of α-synuclein. Red arrows indicate same vesicle identity at t_1 and t_2. (Scale bar: 2 μm.) (*B*) Fluorescence intensity of individual DOPG (blue) and DOPS (red) vesicles before the time of α-synuclein addition (t_1) and up to 40 s (t_2) after addition. The lines are linear fits to the plotted data points, and the shaded area corresponds to the mean square error of the fit. (*C*) A histogram of the relative change in fluorescence intensity between times t_1 and t_2 for individual DOPG and DOPS vesicles. (*D*) Fluorescence intensity profile for cross-section of an individual DOPG vesicle recorded at times t_1 and t_2. A corresponding graph for DOPS shows no difference between t_1 and t_2. (*E*) The change in cross-section FWHM for >100 DOPG and DOPS vesicles.

incubation with α-synuclein at a lipid to protein molar ratio of 5:1. It cannot be excluded that the increase in vesicle size is, in this case, also influenced by vesicle aggregation and fusion, as previously reported for suspended anionic vesicles (47), but the observed up to twofold increase in size is not expected to be accompanied by a pronounced reduction in scattering intensity unless there was a dramatic change in the shape of the vesicles (*SI Appendix*, section 5 and Fig. S11).

Calcein Leakage Is Induced upon Interaction of α-Synuclein with Tethered DOPG Vesicles. The light-scattering measurements of individual vesicles reported here indicate that the interaction between α-synuclein and DOPG lipids leads to stepwise remodeling of the vesicle structure. This process is expected to be preceded by content leakage due to pore formation or membrane thinning, which may occur far earlier than or in parallel with global changes in the vesicle structure. To clarify this aspect, we assessed membrane integrity via calcein leakage from individual DOPG and DOPS vesicles (Fig. 5*A*) at a calcein concentration inside the vesicles (30 mM) where self-quenching is insignificant. Addition of α-synuclein to a sample containing immobilized, calcein-containing DOPG vesicles resulted in a loss of fluorescence signal (Fig. 5*B* and Movie S3), while, for DOPS vesicles, the fluorescence intensity remained more or less unchanged throughout the analyzed time frame (Fig. 5*C*). Similarly, whereas DOPG vesicles displayed the same drop in scattering intensity as previously observed upon α-synuclein addition (Movie S3), the scattering signal for DOPS vesicles remained unchanged (Movie S4). Interestingly, the decrease in scattering and the change in calcein fluorescence were essentially temporarily synchronized (Fig. 5*C*), demonstrating that there is insignificant leakage prior to the actual vesicle collapse. This thus implies that it is the vesicle remodeling, resulting in extensive membrane rupture, that allows for the complete exchange of content between vesicles and the surrounding environment.

Discussion

One of the most striking outcomes from this study is the remarkable difference in the interaction of α-synuclein with membranes composed of PG and PS, two negatively charged lipids. DOPG vesicles collapse into disperse and/or anisotropic patches, whereas DOPS vesicles are significantly less affected. Notably, this difference could not be identified using ensemble-averaging QCM-D and SPR methods but emerged from combined fluorescence and label-free scattering microscopy investigations of single vesicles. It is well established that α-synuclein binds to negatively charged membranes via electrostatic interactions mediated by its N-terminal region, resulting in conformational changes from unordered to α-helix structure (23, 28, 48, 49). The negatively charged phosphate group of DOPS is bound to the polar headgroup serine that has both a positive (NH_3^+) and a negative (COO^-) charge, whereas the PG headgroup is uncharged. The negative charge on PG is, instead, due to the phosphate moiety that binds the polar headgroup with the glycerol. Previously, we observed that α-synuclein, adopted an α-helix structure upon binding to DOPS and DOPG vesicles, but that a higher lipid-to-protein ratio, indicative of larger binding surface area per protein, was needed to attain the maximum helicity content for DOPS (28). The α-synuclein helix is thought to lay flat on the vesicle surface, although partial penetration into the membrane space has also been suggested (10, 50–53). Membrane leakage and structural remodeling as observed in our work require membrane insertion, suggesting not only that differences in the nature and organization of the lipid headgroups do influence membrane-induced helical transition of α-synuclein but also that the N-terminal region of the protein is inserted deeper into DOPG than DOPS vesicle membranes (28).

However, differences in the lipid headgroup alone are not sufficient to explain the far-reaching different effects that α-synuclein has on DOPG membranes compared to DOPS. Considering the lipid bilayer properties, we note that X-ray diffraction and NMR studies showed a higher molecular order in the polar headgroup region of DOPS relative to DOPG in lamellar liquid crystalline phase (54). This fact, together with

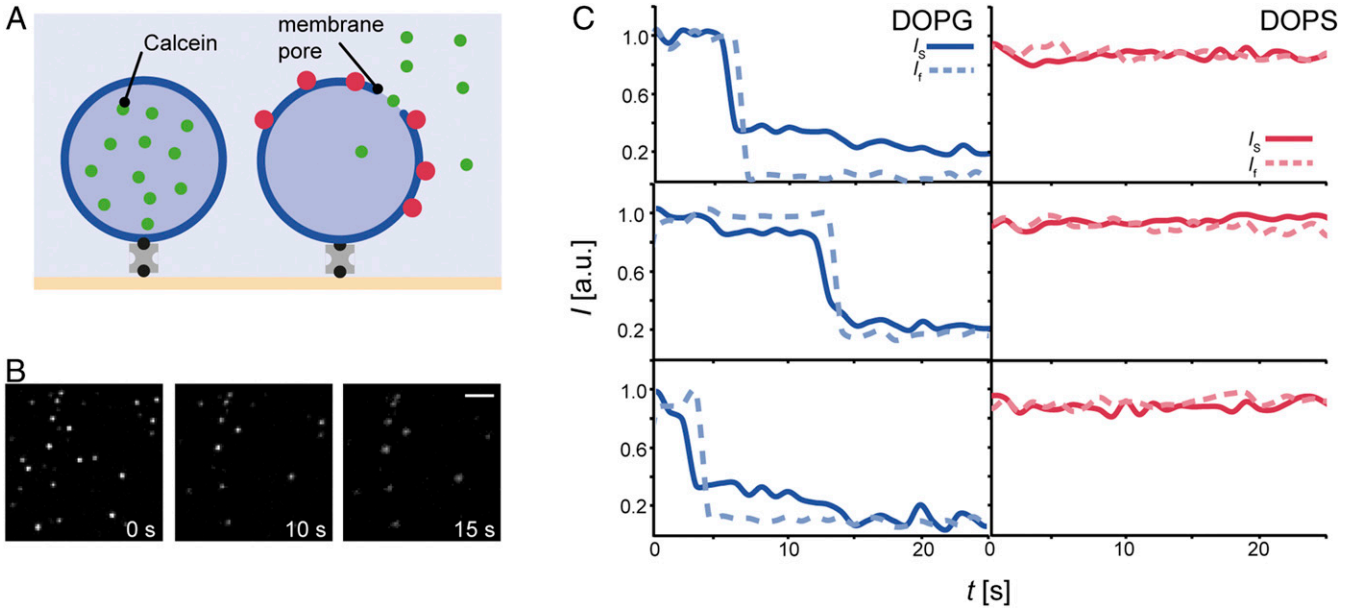

Fig. 5. Single-vesicle calcein leakage assay. (*A*) Schematic illustration of the assay. Vesicles are fluorescently labeled by encapsulated calcein (at a concentration at which the self-quenching effect is not severe). Membrane permeabilization results in calcein release and thus in vesicle fluorescence drop. (*B*) Fluorescence micrographs showing calcein containing vesicles at different time points after addition of α-synuclein. (Scale bar: 2 μm.) (*C*) Normalized fluorescence (dashed lines) and scattering (solid lines) intensity traces for DOPG (blue) and DOPS (red) after addition of α-synuclein at $t = 0$.

observations that α-synuclein binds with greater affinity to model membranes with low lipid density, high curvature, and/or those containing inhomogeneities (17, 26, 55, 56), is consistent with favorable interaction with DOPG membranes over DOPS, including deeper insertion into DOPG bilayers. In addition, previous studies have reported that α-synuclein induces imperfections by lowering membrane rigidity and diffusivity (57, 58), suggesting that dynamic inhomogeneities in the structure of the lipid bilayer will likely be enhanced by α-synuclein binding, resulting in membrane alterations that may promote further protein binding. In the DOPG membranes used here, α-synuclein–induced effects were observed to trigger a chain of events that ultimately promoted asymmetric vesicle collapse in close proximity to the supporting surface and release of vesicle content.

An additional prominent aspect of our results is that a low number of α-synuclein molecules is required to produce far-reaching structural changes in individual vesicles. A tentative explanation for this effect is early emergence of discrete membrane regions with high (local) α-synuclein density that act as nucleation sites for the observed membrane structural changes. This interpretation is supported by the fact that, at low α-synuclein coverage, the structural vesicle remodeling was occasionally observed to occur in multiple distinct steps. Oligomeric α-synuclein has been found to cause lipid membrane disruption, involving membrane thinning, pore formation, and lipid clustering (16, 59–63). In addition, protofibrillar α-synuclein species were reported to affect the integrity of surface-adsorbed membranes containing anionic phospholipids (64). Regarding α-synuclein monomers, they were previously described to cause leakage of encapsulated molecules from DOPG vesicles only if present at high concentrations: Membrane permeabilization was observed at a protein concentration of 23 μM and a lipid:protein molar ratio of 28, but there was no leakage at higher ratios (no effect at a lipid:protein ratio of 81) (65). Using our single-vesicle resolution technique, we could detect membrane structural changes and vesicle leakage at low nanomolar concentrations of monomeric α-synuclein and lipid:protein ratios higher than on the order of 10^3. Importantly, we also revealed that α-synuclein induced structural remodeling of DOPG vesicles that occurred in a stepwise fashion (often single step but sometimes multiple steps) and at low α-synuclein concentration. Although suspended α-synuclein does not aggregate into amyloid fibrils under the conditions used here, our data are consistent with α-synuclein monomers clustering on the membrane surfaces such that structural alterations and leakage are initiated by less than a hundred protein molecules per vesicle. From inspection of the fluorescence micrographs, it is clear that these structural changes occur without complete disintegration and removal of lipid material from the surface, as previously observed for, for example, pore-forming antimicrobial peptides (35).

In conclusion, we have demonstrated that the molecular events that appear to control how α-synuclein interacts with different anionic lipid vesicles are difficult to pinpoint from ensemble-averaging methods alone, regardless of whether they are based on bulk or surface-based measurements. However, combining ensemble-averaging methods with single-vesicle approaches that reveal information about structure and integrity of individual lipid vesicles successfully showed that α-synuclein induces membrane disruption through lipid-specific interactions that (already at low α-synuclein binding) result in abrupt single-step or multistep asymmetric vesicle collapse that takes place simultaneously with content release. It is of interest that this scenario differs from those observed in the case of antimicrobial peptides, where the vesicle rupture is usually preceded by the pore formation and occurs gradually or, in the case of pore formation in giant vesicles, with subsequent gradual disintegration of the vesicles (30–35). This difference can qualitatively be explained by taking the specifics of these systems into account. In particular, antimicrobial peptides form small pores, and one or a few of such peptides are not able to induce vesicle rupture (30). In contrast, α-synuclein is a larger protein and tends to aggregate on the surface of lipid bilayers (66). Our results for large unilamellar vesicles are consistent with initial α-synuclein monomer binding being accompanied by rapid clustering of additional α-synuclein monomers, which appears to cause leakage via vesicle rupture rather than classical pore formation associated with antimicrobial peptides. Together, these observations provide mechanistic insights for how amyloid-forming proteins perturb lipid membranes in general, and nanosized vesicles in particular, and may be directly related to aberrant behavior of monomeric α-synuclein in vivo.

Materials and Methods

Materials. DOPG and DOPS chloroform solutions, and DSPE-PEG(2000) Biotin (1,2-distearoyl-sn-glycero-3-phosphoethanolamine-*N*-[biotinyl(poly-ethyleneglycol)-2000], ammonium salt) were from Avanti Polar Lipids. Rhodamine DHPE was from Invitrogen. Sodium phosphate monobasic (NaH_2PO_4; ≥99%), sodium phosphate dibasic (Na_2HPO_4; ≥99.0%), ethylenediaminetetraacetic acid (EDTA; ≥99%), NeutrAvidin, and calcein were purchased from Sigma-Aldrich.

Protein Expression and Purification. Human α-synuclein construct was expressed in *Escherichia coli* BL21 (DE3) (Novagen) cells at 37 °C in lysogeny broth media containing 100 μg/mL carbenicillin. After the bacteria suspension reached an optical density at 600 nm of 0.6, the cells were induced with 1 mM isopropyl β-D-1-thiogalactopyranoside and incubated overnight at 25 °C. Bacterial pellets were resuspended in 20 mM Tris·HCl buffer pH 8.0 containing protease inhibitor mixture (Roche) and sonicated on an ice bath using a sonicator probe in pulse mode. The lysate was treated with universal nuclease (Pierce) for 15 min at room temperature and heated to 90 °C for 10 min followed by centrifugation at 15,000 × *g* for 30 min. The supernatant was filtered through a 0.2-μm filter, loaded on to a preequilibrated 5-mL HiTrap Q FF anion exchange column (GE Healthcare), and eluted by linear gradient with 1 M NaCl in 20 mM Tris·HCl buffer pH 8.0. Fractions containing α-synuclein were concentrated with Ultra-15 Ultracel 10KDa centrifugal filter devices (Millipore), applied to a Hiload 16/600 Superdex 75-pg column (GE Healthcare), and eluted with 20 mM Tris-sulfate buffer pH 7.4. The protein fraction was flash frozen in liquid nitrogen and stored at −80 °C. Before each experiment, the protein was gel filtered using a Superdex 75 10/300 GL column (GE Healthcare) and eluted with 20 mM phosphate buffer, 1 mM EDTA, pH 6.5 in order to exchange the buffer and ensure the presence of monomers only. The protein concentration was determined by ultraviolet (UV)-visible spectroscopy (ε_{280} = 5,960 $M^{-1}{\cdot}cm^{-1}$).

Lipid Vesicle Preparation. Vesicles were prepared by the lipid film hydration and extrusion method. Appropriate volumes of chloroform solution of DOPG or DOPS were transferred to a round-bottomed flask. Biotinylated vesicles were prepared by mixing 1% of the total lipid mass of DSPE-PEG(2000) Biotin (dissolved in methanol) with DOPG or DOPS in the organic solution. In the case of fluorescently labeled vesicles, rhodamine DHPE was also added (1 wt %) to the vesicles. The organic solvents were removed by rotary evaporation, and the resultant film was dried under vacuum for at least 3 h, hydrated with 20 mM phosphate buffer, 1 mM EDTA, pH 6.5, and vortexed for 10 min. The size of the vesicles was reduced by extrusion using Avestin LiposoFast-Basic extruder and 100-nm-pore-size polycarbonate membranes.

QCM-D. All measurements were performed using a Q-Sense E4 (Biolin Scientific) and SiO_2-coated crystals (Q-Sense, Biolin Scientific), cleaned by sonication (Elmasonic, Elma Schmidbauer GmbH) with sodium dodecyl sulfate (SDS, Sigma-Aldrich) and ultrapure H_2O (Synergy systems, Merck Millipore Corporation) prior to drying with a flow of N_2 and UV/Ozone treatment (UV/Ozone Procleaner Plus, BioForce Nanosciences) for 30 min. The baseline was normalized with the phosphate buffer described above prior to each experiment. At the start of the experiment, the sensor surface was coated with 10 μg/mL PLL-g-PEG (PLL (20)-g[3.5]-PEG (2) from SuSOS AG), with 0.25% or 1% of the PLL-g-PEG functionalized with biotin (PLL (20)-g[3.5]-PEG (2)/PEGbiotin(3.4) 50% from SuSOS AG). When saturation was reached, NeutrAvidin was added at 10 μg/mL concentration until no further binding was observed. To this, vesicles (100 μg/mL lipid concentration) containing 1% biotinylated lipids were added until reaching saturation

followed by α-synuclein. The sample cells were rinsed with buffer between every addition.

MP-SPR. The dual-wavelength surface plasmon resonance (SPR) measurements were performed with an SPR Navi 220A (BioNavis) on SiO_2-coated chips (SPR102-SIO2, BioNavis), first cleaned by rinsing in 10 mM SDS with subsequent rinsing in ultrapure water. After rinsing, the chips were dried in nitrogen flow and then treated with UV/Ozone (UV/Ozone Procleaner Plus, BioForce Nanosciences, Inc.) for 30 min. After the washing procedure, the chip was then docked in the SPR instrument and primed with circulating buffer at 20 μL/min. The chip was coated with PLL-g-PEG-biotin:PLL-g-PEG and vesicles tethered through NeutrAvidin as described for QCM-D experiments, and SPR was monitored at wavelengths 670 and 785 nm for a scanning interval between ∼65° and 78°. The measurements were performed at 21 °C.

Waveguide Chip Fabrication and Surface Modification. The fabrication of the waveguide device is described in detail elsewhere (67). Briefly, a 400-nm-thick silica core layer (spin-on-glass, IC1-200 from Futurrex, Inc.), embedded in a 7-μm-thick cladding layer of fluorinated polymer (CYTOP, CTX-809AP2 from AGC Chemicals, ASAHI Glass Co., Ltd.), was fabricated on a standard Si(100) 4-inch wafer. Square wells with a side length of 2 mm were formed in the cladding layer by reactive etching exposing the core layer of the waveguide. Before being used for experiments, the chips were treated for 15 min in O_2 plasma (Harrick Plasma cleaner, 30 W), followed by cleaning in 2 M sulfuric acid (H_2SO_4) for 30 min before subsequent extensive rinsing in ultrapure water and drying in nitrogen gas. Before the experiments, cleaned waveguide chips were incubated first with PLL-g-PEG (10 μg/mL), of which 1% were modified with biotin, for 20 min. The chips were then rinsed with ultrapure water. Any remaining water was removed using a pipette (a small = 5-μL drop remained on top of the sample area of the waveguide). After this, NeutrAvidin was added and kept for 20 min. The rinsing procedure was repeated before addition of 20 μL of buffer. Vesicles (10 μg/mL lipid concentration) were then added under observation in the microscope. When a sufficient amount of vesicles had bound to the surface, the binding process was stopped by aspirating the vesicle solution with a pipette, while replacing it with an equal volume of buffer. Movie recordings were started before adding a small volume of α-synuclein using a pipette to a final α-synuclein concentration of 200 nM. After addition, the system was mixed using a pipette.

Microscopy Setup. All waveguide measurements were carried out on an Olympus BX61 upright microscope equipped with a 100×, NA 1.0 Leica water-dipping objective and a Hamamatsu ORCA Flash 4.0 V2 scientific complementary metal oxide semiconductor (CMOS) camera connected to a Hamamatsu W-VIEW GEMINI image splitter containing specific filter cubes (dichroic mirror: 562 nm; fluorescence band-pass: 590/50; and scattering band-pass: 535/50) allowing for simultaneous acquisition of fluorescence and scattering signals. A functionalized waveguide chip was placed under the objective, and single-mode, 532-nm, TE polarized light (from fiber-coupled NANO 250 [Qioptiq, Inc.] Laser) was butt-coupled into the chip via a single-mode fiber that was carefully aligned to the facet of the waveguide using a manual three-axis translational stage. Once aligned, a solution containing vesicles was exposed to the chip, and the surface binding of vesicles was monitored in real time. When a suitable surface coverage had been reached, the chip was rinsed with buffer and subsequently exposed to α-synuclein. For further details on the waveguide chip and experimental setup, see ref. 67.

Single-Vesicle Scattering and Fluorescence Measurements. Surface-tethered lipid vesicle samples were prepared as described above. The sample was imaged using the microscope setup described above with a 100-ms integration time at 0.1 frames per s. Scattering and fluorescence signals were recorded simultaneously by using an image-splitting device. Recorded images were analyzed in ImageJ. First, the corresponding fluorescence and scattering images were aligned using a built-in alignment module in ImageJ. Single-vesicle intensities were then obtained by integrating the intensity within an area confining the vesicle signal. This area was defined at the end of the recording, for the fluorescence data (signal footprint growing with time), and at the beginning of the recording, for the scattering data (signal footprint remaining essentially constant with time). Mean background intensity per pixel was evaluated locally for each vesicle and subtracted from its integrated scattering and fluorescence intensity.

Leakage Assay. Biotinylated vesicles with encapsulated calcein at a concentration of 30 mM, at which the self-quenching effect is sufficiently weak to enable the individual vesicles to be detectable, were prepared by hydrating the lipid film with phosphate buffer containing the dye. Calcein was dissolved in alkaline environment (1 M NaOH) and then diluted with phosphate buffer (20 mM phosphate buffer, 1 mM EDTA, pH 6.5). The vesicles were vortexed, extruded, and immobilized on the chip surface as described previously. Free calcein was removed by washing the immobilized vesicles with phosphate buffer before adding α-synuclein. Fluorescence emission was detected using a 100-ms integration time. An image was recorded every 2 s in order to allow prolonged recording times without causing substantial bleaching of the dyes in the sample. It should be noted that the presence of calcein inside vesicles has an apparent negative impact on the ability of α-synuclein to interact with the lipid membranes used in this study. To obtain a similar level of interaction, as measured by QCM-D (presented in *SI Appendix*), a 10-fold higher α-synuclein concentration was required. This means that quantitative results obtained using the different methods are not directly comparable.

Data availability. All data and procedures are provided in the manuscript and *SI Appendix*.

ACKNOWLEDGMENTS. This work was supported by the Knut and Alice Wallenberg Foundation, Swedish Research Council, and Chalmers University Area of Advance Seed Grant. We thank Ranjeet Kumar (Department of Biology and Biological Engineering, Chalmers University of Technology) for expression and purification of α-synuclein. This work was performed in part at the Chalmers Material Analysis Laboratory (CMAL).

1. A. John, W. van der Pluijm, The global prevalence of Parkinson's disease over the next ten years. *Ann. Neurol.* **84**, S219 (2018).
2. A. Elkouzi, V. Vedam-Mai, R. S. Eisinger, M. S. Okun, Emerging therapies in Parkinson disease-Repurposed drugs and new approaches. *Nat. Rev. Neurol.* **15**, 204–223 (2019).
3. M. S. Goldberg, P. T. Lansbury Jr., Is there a cause-and-effect relationship between alpha-synuclein fibrillization and Parkinson's disease? *Nat. Cell Biol.* **2**, E115–E119 (2000).
4. M. G. Spillantini *et al*., α-synuclein in Lewy bodies. *Nature* **388**, 839–840 (1997).
5. V. N. Uversky, Neuropathology, biochemistry, and biophysics of α-synuclein aggregation. *J. Neurochem.* **103**, 17–37 (2007).
6. M. H. Polymeropoulos *et al*., Mutation in the α-synuclein gene identified in families with Parkinson's disease. *Science* **276**, 2045–2047 (1997).
7. G. Fusco *et al*., Structural basis of synaptic vesicle assembly promoted by α-synuclein. *Nat. Commun.* **7**, 12563 (2016).
8. K. K. Dev, K. Hofele, S. Barbieri, V. L. Buchman, H. van der Putten, Part II: α-synuclein and its molecular pathophysiological role in neurodegenerative disease. *Neuropharmacology* **45**, 14–44 (2003).
9. L. B. Lassen, L. Reimer, N. Ferreira, C. Betzer, P. H. Jensen, Protein partners of α-synuclein in health and disease. *Brain Pathol.* **26**, 389–397 (2016).
10. D. Eliezer, E. Kutluay, R. Bussell, G. Browne, "Conformational properties of α-synuclein in its free and lipid-associated states" in *J. Mol. Biol.*, (2001), Vol. 307, pp. 1061–1073.
11. A. Iwai *et al*., The precursor protein of non-A β component of Alzheimer's disease amyloid is a presynaptic protein of the central nervous system. *Neuron* **14**, 467–475 (1995).
12. L. Maroteaux, J. T. Campanelli, R. H. Scheller, Synuclein: A neuron-specific protein localized to the nucleus and presynaptic nerve terminal. *J. Neurosci.* **8**, 2804–2815 (1988).
13. H.-J. Lee, C. Choi, S.-J. Lee, Membrane-bound α-synuclein has a high aggregation propensity and the ability to seed the aggregation of the cytosolic form. *J. Biol. Chem.* **277**, 671–678 (2002).
14. F. Miraglia, A. Ricci, L. Rota, E. Colla, Subcellular localization of alpha-synuclein aggregates and their interaction with membranes. *Neural Regen. Res.* **13**, 1136–1144 (2018).
15. B. Mollenhauer *et al*., Direct quantification of CSF alpha-synuclein by ELISA and first cross-sectional study in patients with neurodegeneration. *Exp. Neurol.* **213**, 315–325 (2008).
16. N. P. Reynolds *et al*., Mechanism of membrane interaction and disruption by α-synuclein. *J. Am. Chem. Soc.* **133**, 19366–19375 (2011).
17. M. M. Ouberai *et al*., α-Synuclein senses lipid packing defects and induces lateral expansion of lipids leading to membrane remodeling. *J. Biol. Chem.* **288**, 20883–20895 (2013).
18. E. Hellstrand *et al*., Adsorption of α-synuclein to supported lipid bilayers: Positioning and role of electrostatics. *ACS Chem. Neurosci.* **4**, 1339–1351 (2013).
19. A. R. Braun *et al*., α-Synuclein induces both positive mean curvature and negative Gaussian curvature in membranes. *J. Am. Chem. Soc.* **134**, 2613–2620 (2012).
20. H. Chaudhary, A. N. Stefanovic, V. Subramaniam, M. M. Claessens, Membrane interactions and fibrillization of α-synuclein play an essential role in membrane disruption. *FEBS Lett.* **588**, 4457–4463 (2014).

21. T. Logan, J. Bendor, C. Toupin, K. Thorn, R. H. Edwards, α-Synuclein promotes dilation of the exocytotic fusion pore. *Nat. Neurosci.* **20**, 681–689 (2017).
22. A. Iyer, M. M. A. E. Claessens, Disruptive membrane interactions of alpha-synuclein aggregates. *Biochim. Biophys. Acta. Proteins Proteomics* **1867**, 468–482 (2019).
23. C. M. Pfefferkorn, Z. Jiang, J. C. Lee, Biophysics of α-synuclein membrane interactions. *Biochim. Biophys. Acta* **1818**, 162–171 (2012).
24. C. H. Westphal, S. S. Chandra, Monomeric synucleins generate membrane curvature. *J. Biol. Chem.* **288**, 1829–1840 (2013).
25. Z. Jiang, M. de Messieres, J. C. Lee, Membrane remodeling by α-synuclein and effects on amyloid formation. *J. Am. Chem. Soc.* **135**, 15970–15973 (2013).
26. V. V. Shvadchak, L. J. Falomir-Lockhart, D. A. Yushchenko, T. M. Jovin, Specificity and kinetics of α-synuclein binding to model membranes determined with fluorescent excited state intramolecular proton transfer (ESIPT) probe. *J. Biol. Chem.* **286**, 13023–13032 (2011).
27. M. Stöckl, P. Fischer, E. Wanker, A. Herrmann, Alpha-synuclein selectively binds to anionic phospholipids embedded in liquid-disordered domains. *J. Mol. Biol.* **375**, 1394–1404 (2008).
28. J. Kiskis, I. Horvath, P. Wittung-Stafshede, S. Rocha, Unraveling amyloid formation paths of Parkinson's disease protein α-synuclein triggered by anionic vesicles. *Q. Rev. Biophys.* **50**, e3 (2017).
29. S. M. Butterfield, H. A. Lashuel, Amyloidogenic protein-membrane interactions: Mechanistic insight from model systems. *Angew. Chem. Int. Ed. Engl.* **49**, 5628–5654 (2010).
30. S. Guha, J. Ghimire, E. Wu, W. C. Wimley, Mechanistic landscape of membrane-permeabilizing peptides. *Chem. Rev.* **119**, 6040–6085 (2019).
31. M. P. D. Cabrera *et al*., New insight into the mechanism of action of wasp mastoparan peptides: Lytic activity and clustering observed with giant vesicles. *Langmuir* **27**, 10805–10813 (2011).
32. M. Z. Islam, J. M. Alam, Y. Tamba, M. A. Karal, M. Yamazaki, The single GUV method for revealing the functions of antimicrobial, pore-forming toxin, and cell-penetrating peptides or proteins. *Phys. Chem. Chem. Phys.* **16**, 15752–15767 (2014).
33. Y. Tamba, M. Yamazaki, Single giant unilamellar vesicle method reveals effect of antimicrobial peptide magainin 2 on membrane permeability. *Biochemistry* **44**, 15823–15833 (2005).
34. J. H. Vanzanten, H. G. Monbouquette, Characterization of vesicles by classical light-scattering. *J. Colloid Interface Sci.* **146**, 330–336 (1991).
35. S. R. Tabaei, M. Rabe, V. P. Zhdanov, N.-J. Cho, F. Höök, Single vesicle analysis reveals nanoscale membrane curvature selective pore formation in lipid membranes by an antiviral α-helical peptide. *Nano Lett.* **12**, 5719–5725 (2012).
36. J. A. Jackman, R. Saravanan, Y. Zhang, S. R. Tabaei, N. J. Cho, Correlation between membrane partitioning and functional activity in a single lipid vesicle assay establishes design guidelines for antiviral peptides. *Small* **11**, 2372–2379 (2015).
37. B. Agnarsson *et al*., Evanescent light-scattering microscopy for label-free interfacial imaging: From single sub-100 nm vesicles to live cells. *ACS Nano* **9**, 11849–11862 (2015).
38. B. Agnarsson, H. K. Wayment-Steele, F. Höök, A. Kunze, Monitoring of single and double lipid membrane formation with high spatiotemporal resolution using evanescent light scattering microscopy. *Nanoscale* **8**, 19219–19223 (2016).
39. J. Andrecka, K. M. Spillane, J. Ortega-Arroyo, P. Kukura, Direct observation and control of supported lipid bilayer formation with interferometric scattering microscopy. *ACS Nano* **7**, 10662–10670 (2013).
40. G. Ohlsson, A. Tigerström, F. Höök, B. Kasemo, Phase transitions in adsorbed lipid vesicles measured using a quartz crystal microbalance with dissipation monitoring. *Soft Matter* **7**, 10749–10755 (2011).
41. E. Reimhult, C. Larsson, B. Kasemo, F. Höök, Simultaneous surface plasmon resonance and quartz crystal microbalance with dissipation monitoring measurements of biomolecular adsorption events involving structural transformations and variations in coupled water. *Anal. Chem.* **76**, 7211–7220 (2004).
42. D. L. M. Rupert *et al*., Dual-wavelength surface plasmon resonance for determining the size and concentration of sub-populations of extracellular vesicles. *Anal. Chem.* **88**, 9980–9988 (2016).
43. C. Osman, D. R. Voelker, T. Langer, Making heads or tails of phospholipids in mitochondria. *J. Cell Biol.* **192**, 7–16 (2011).
44. S. E. Horvath, G. Daum, Lipids of mitochondria. *Prog. Lipid Res.* **52**, 590–614 (2013).
45. L. Lim, M. R. Wenk, "Neuronal membrane lipids – their role in the synaptic vesicle cycle" in *Handbook of Neurochemistry and Molecular Neurobiology: Neural Lipids*, A. Lajtha, G. Tettamanti, G. Goracci, Eds. (Springer, Boston, MA, 2009), pp. 223–238.
46. H. Zhao, P. H. Brown, P. Schuck, On the distribution of protein refractive index increments. *Biophys. J.* **100**, 2309–2317 (2011).
47. W. C. Wimley, Describing the mechanism of antimicrobial peptide action with the interfacial activity model. *ACS Chem. Biol.* **5**, 905–917 (2010).
48. T. Bartels *et al*., The N-terminus of the intrinsically disordered protein α-synuclein triggers membrane binding and helix folding. *Biophys. J.* **99**, 2116–2124 (2010).
49. E. Rhoades, T. F. Ramlall, W. W. Webb, D. Eliezer, Quantification of α-synuclein binding to lipid vesicles using fluorescence correlation spectroscopy. *Biophys. J.* **90**, 4692–4700 (2006).
50. C. R. Bodner, C. M. Dobson, A. Bax, Multiple tight phospholipid-binding modes of alpha-synuclein revealed by solution NMR spectroscopy. *J. Mol. Biol.* **390**, 775–790 (2009).
51. J. Dedic, S. Rocha, H. I. Okur, P. Wittung-Stafshede, S. Roke, Membrane-Protein-Hydration interaction of alpha-synuclein with anionic vesicles probed via angle-resolved second-harmonic scattering. *J. Phys. Chem. B* **123**, 1044–1049 (2019).
52. G. Fusco *et al*., Direct observation of the three regions in α-synuclein that determine its membrane-bound behaviour. *Nat. Commun.* **5**, 3827 (2014).
53. C. C. Jao, B. G. Hegde, J. Chen, I. S. Haworth, R. Langen, Structure of membrane-bound alpha-synuclein from site-directed spin labeling and computational refinement. *Proc. Natl. Acad. Sci. U.S.A.* **105**, 19666–19671 (2008).
54. G. Lindblom *et al*., Effect of head-group structure and counterion condensation on phase equilibria in anionic phospholipid-water systems studied by 2H, 23Na, and 31P NMR and x-ray diffraction. *Biochemistry* **30**, 10938–10948 (1991).
55. B. Nuscher *et al*., α-synuclein has a high affinity for packing defects in a bilayer membrane: A thermodynamics study. *J. Biol. Chem.* **279**, 21966–21975 (2004).
56. E. R. Middleton, E. Rhoades, Effects of curvature and composition on α-synuclein binding to lipid vesicles. *Biophys. J.* **99**, 2279–2288 (2010).
57. A. Iyer, N. O. Petersen, M. M. Claessens, V. Subramaniam, Amyloids of alpha-synuclein affect the structure and dynamics of supported lipid bilayers. *Biophys. J.* **106**, 2585–2594 (2014).
58. A. Iyer, N. Schilderink, M. M. A. E. Claessens, V. Subramaniam, Membrane-bound alpha-synuclein clusters induce impaired lipid diffusion and increased lipid packing. *Biophys. J.* **111**, 2440–2449 (2016).
59. R. Kayed *et al*., Common structure of soluble amyloid oligomers implies common mechanism of pathogenesis. *Science* **300**, 486–489 (2003).
60. H. A. Lashuel *et al*., Alpha-synuclein, especially the Parkinson's disease-associated mutants, forms pore-like annular and tubular protofibrils. *J. Mol. Biol.* **322**, 1089–1102 (2002).
61. B. Winner *et al*., In vivo demonstration that alpha-synuclein oligomers are toxic. *Proc. Natl. Acad. Sci. U.S.A.* **108**, 4194–4199 (2011).
62. L. Giehm, D. I. Svergun, D. E. Otzen, B. Vestergaard, Low-resolution structure of a vesicle disrupting α-synuclein oligomer that accumulates during fibrillation. *Proc. Natl. Acad. Sci. U.S.A.* **108**, 3246–3251 (2011).
63. B. D. van Rooijen, M. M. Claessens, V. Subramaniam, Lipid bilayer disruption by oligomeric alpha-synuclein depends on bilayer charge and accessibility of the hydrophobic core. *Biochim. Biophys. Acta* **1788**, 1271–1278 (2009).
64. M. J. Volles *et al*., Vesicle permeabilization by protofibrillar alpha-synuclein: Implications for the pathogenesis and treatment of Parkinson's disease. *Biochemistry* **40**, 7812–7819 (2001).
65. M. J. Volles, P. T. Lansbury Jr., Vesicle permeabilization by protofibrillar alpha-synuclein is sensitive to Parkinson's disease-linked mutations and occurs by a pore-like mechanism. *Biochemistry* **41**, 4595–4602 (2002).
66. H. Chaudhary, V. Subramaniam, M. M. A. E. Claessens, Direct visualization of model membrane remodeling by α-synuclein fibrillization. *ChemPhysChem* **18**, 1620–1626 (2017).
67. B. Agnarsson, M. Mapar, M. Sjöberg, M. Alizadehheidari, F. Höök, Low-temperature fabrication and characterization of a symmetric hybrid organic-inorganic slab waveguide for evanescent light microscopy. *Nano Futures* **2**, 25007 (2018).